Nanoscale

PAPER

View Article Online
View Journal | View Issue



Cite this: *Nanoscale*, 2023, **15**, 10360

# Understanding spatiotemporal mechanical behavior, viscoelasticity, and functions of stem cell-derived cardiomyocytes†

Lihua Lou, [a] Alberto Sesena Rubfiaro, [b] Jin He [b] and Arvind Agarwal *[a]

Understanding myocytes' spatiotemporal mechanical behavior and viscoelasticity is a long-standing challenge as it plays a critical role in regulating structural and functional homeostasis. To probe the time-dependent viscoelastic behaviors of cardiomyocytes with cross-linked polymer networks, we measure stem cell-derived cardiomyocyte's (hiPSC-CM) deformation, adhesion, and contractility using atomic force microscopy (AFM) nanoindentation, fluidic micropipette, and digital image correlation (DIC). Our results show a cytoplasm load of 7–14 nN, a de-adhesion force of 0.1–1 nN, and an adhesion force between two hiPSC-CMs of 50–100 nN with an interface energy of 0.45 pJ. Based on the load–displacement curve, we model its dynamic viscoelasticity and discover its intimate associations with physiological properties. Cell detaching and contractile modeling demonstrate cell–cell adhesion and beating related strains manifesting viscoelastic behavior, highlighting viscoelasticity plays the primary role in governing hiPSC-CM spatiotemporal mechanics and functions. Overall, this study provides valuable information about the mechanical properties, adhesion behaviors, and viscoelasticity of single hiPSC-CM, shedding light on mechanical–structure relationships and their dynamic responses to mechanical stimuli and spontaneous contraction.

Received 3rd April 2023,
Accepted 4th June 2023

DOI: 10.1039/d3nr01553j

rsc.li/nanoscale



## Introduction

The capability to quantify a single cardiomyocyte's mechanical behavior[1,2] is critical for elucidating cardiac biological and pharmaceutical questions.[3,4] It promises to decipher myocyte mechanotransduction,[5] physiological development,[6] and pathological mechanism.[3] *In vitro* mechanical test platform allows measuring the influences of bio-environment factors, cardiovascular drugs,[7] substrate topology/stiffness,[8–11] aging, and pH on the viscoelasticity, adhesion,[12] and beating mechanics[13,14] of hiPSC-CM. Compared to 2D or 3D cardiac microbundles or patches,[15–18] this platform is simple and has data precision due to controllable cell quality and technical maturity.

Despite the significant advances in single-cell mechanics measuring tools, the studies are limited to its force and strain responses,[1] deformation–disease relationship,[7] substrate effects,[8,9] differentiation-mechanics association,[19] mutation-adhesion mechanism,[20] and disease detection.[21] Moreover, most of the studies focused on semi-quantitative or quantitative tools[6,22,23] in detecting cell mechanical properties and intercellular adhesions or the functions of genes,[24] proteins/receptors,[25] and growth factor signaling[26] from the biological and chemical perspectives. However, the studies of single cardiomyocytes' mechanics and viscoelasticity are limited. Viscoelasticity indicates instantaneous responsiveness with velocity dependency behavior when faced with external deformation.[27,28] In theory, cardiomyocytes exhibit unique viscoelasticity and adaptability attributed to high contractility and arrangement of myofilaments and cytoskeleton.[8] Therefore, fundamental research of mechanics and viscoelasticity of single cardiomyocyte with complex structure and functional behaviors can provide fundamental insights into (1) the structure–contractility–viscoelasticity relationship; (2) the underlying disease mechanism; (3) developing novel therapies; (4) fabricating fully functional cardiac patches.

Existing studies of single cardiomyocyte mechanics can be categorized into two branches: (1) contractile mechanics; (2) mechanics measurement and modeling. Iribe *et al.*[29] studied the effects of external stretching load on a single isolated cardiomyocyte end-systolic force. The results demonstrated thin filaments' (in)activation exhibiting velocity- and load-depen-

[a]*Mechanical and Materials Engineering, School of Biomedical, Materials and Mechanical Engineering (SBMME), College of Engineering and Computing, Florida International University, 10555 West Flagler Street, Miami, FL 33174, USA. E-mail: agarwala@fiu.edu*

[b]*Department of Physics, Florida International University, Miami, FL 33174, USA*

† Electronic supplementary information (ESI) available. See DOI: https://doi.org/10.1039/d3nr01553j

dent. Ribeiro *et al.*[8] investigated the influences of substrate stiffness and physiological shape on single hiPSC-CM contractility, demonstrating associations between contractility and myofibril maturity metrics. However, the contractility–viscoelasticity relationship remains unclear. As for cardiomyocyte mechanics measurement and modeling, Lieber *et al.*[30] reported the effects of aging on cardiac myocytes' stiffness and its relationship with left ventricular diastolic dysfunction. Deitch *et al.*[31] explored substrate-induced nanomechanical and viscoelastic changes of 2D cultured neonatal rat cardiomyocytes. Lanzicher *et al.*[32] explored the linkages between neonatal rat cardiomyocytes' membrane adhesion and cytoskeletal viscoelastic with mutated lamin A/C gene (LMNA). Zhang *et al.*[33] characterized a single cardiomyocyte cell contractile behavior using a linear dynamic model to explore effects of subcellular structure on cytoskeleton mechanics. However, there is little knowledge regarding the uniqueness of cardiomyocyte viscoelasticity, mechanical, and adhesion roles and mechanisms in maintaining its morphogenesis and regulating functional behaviors. Moreover, the structural–mechanical–functional associations at a single-cell level and the potential application of cell mechanics and related technologies in biological and clinical studies remain unexplored.

This study aimed to explore force-controlled single hiPSC-CM mechanical performance, revealing its dynamic changes in architecture and compositions, including cell membrane, cytoskeleton, and cytoplasm physiological status. We seek to provide insights into hiPSC-CM viscoelasticity, adhesion, cell–cell/cell–substrate communication, spatiotemporal displacements/strains, and mechanotransduction at cell junctions using AFM nanoindentation, fluidic micropipette, and DIC technique. More importantly, we intended to discover the interrelationship among viscoelastic behaviors, surface mechanical properties, adhesion, and beating mechanics. Overall, we targeted to explore fundamental hiPSC-CM mechanical behaviors, structure–contractility–viscoelasticity relationships, and the consequences of these properties for physiological functions. This work has potential practical applications for cardiovascular drug screening and mechanics-disease mechanisms research. Beyond that, the unique structural, mechanical, and adhesion properties of hiPSC-CM are critical for practical applications for cardiovascular drug screening and mechanics-disease mechanisms research.

## Results and discussion

### Single hiPSC-CM mechanical properties

During AFM nanoindentation on living hiPSC-CMs seeded on a glass slide without fixation (Fig. 1A), the probe exerts a force on the cell membrane, cytoskeleton, and cytoplasm to reveal the mechanical response that is illustrated as the load–displacement curve in Fig. 1B. The load–displacement curve consisted of the approaching–loading–unloading–retraction process, where $P_0$ and $P_1$ are the loading curve's start and endpoints. The average indentation depth was ~300 nm, corresponding to a deformation strain ($\varepsilon$) of 0.075–0.12. $\varepsilon$ is calculated using eqn (1):

$$\varepsilon = d/t_{\text{hiPSC-CM}} \quad (1)$$

where $t_{\text{hiPSC-CM}}$ is the thickness of hiPSC-CM (2.5–4 μm[34]). According to Lulevich[35] *et al.*'s study, $0.2 < \varepsilon < 0.3$ and $0.3 < \varepsilon < 0.8$ suggested cell membrane remain impermeable and bursting with stress peaks, respectively. The stress peak(s) displayed on the loading curve, indicating rupture of membrane, a break of cytoskeleton crosslinkers, leakage of cytoplasm, and drop of cell pressure. In this study, there was no stress peak on the loading curve, suggesting hiPSC-CM remained undamaged during and after AFM nanoindentation testing. The loading section includes two regions: (1) an initial contact and bending of the cell membrane (green color) and (2) cytoskeleton and cytoplasm deformation (yellow color). The initial linear stage (Fig. 1C) with a displacement within 10 nm corresponds to the elastic lipid bilayer of 5–10 nm in thickness[2] with a detected cell membrane load of 7–14 nN.

The nonlinear region gradually manifested with displacement higher than 10 nm, attributing to a composite character of sarcomeric cytoskeleton and cytoplasm. Cytoskeletons of intertwined and interlinked actin, microtubules, and intermediate filaments demonstrate nonlinear stiffness and viscoelastic characteristics.[3] Cytoplasm constitutes ~80% water and is treated as a viscoplastic fluid.[2] The combined elastic cell membrane, viscoelastic cytoskeleton, and viscoplastic cytoplasm characteristics were manifested with dominated viscoelasticity with a hysteresis phenomenon, showing as a blue interspace within loading and unloading curves. The dissipation loop, the interspace, shows a dissipated energy of 55.75 ± 7.98% due to heat loss trigged by internal composite macropolymers friction. The dissipated energy was calculated using eqn (2):

$$\text{Dissipated energy}\,(\%) = 1 - \frac{\int_{x1}^{x2} F_{\text{loading}}\mathrm{d}_x}{\int_{x1}^{x2} F_{\text{unloading}}\mathrm{d}_x} \times 100\% \quad (2)$$

where $x1$ and $x2$ are the specific displacements corresponding to the loading curve start ($P_0$) and end ($P_1$) points. The viscoelasticity of cardiomyocytes is intimately linked with their physiological functional properties,[32] including regulation of electrical signaling, cellular differentiation, and gene expression. The linkages are through functional molecules within the cytoskeleton network, intracellular structures, and extracellular matrix, *e.g.*, collagen, elastin, fibronectin, titin, and actin.

Fig. 1D illustrates three probe–sample interaction stages corresponding to the load–displacement curve: (1) approaching stage related to the process of that probe moving toward the sample surface ($P_0$) with a load of 0 N, (2) the loading–unloading stage depicting the direct mechanical interaction of the probe–sample, and (3) the retraction stage tracking adhesion of the probe–sample by detaching the probe from the sample with a load < 0 N.

The reduced elastic modulus ($E'$) of hiPSC-CMs were calculated based on the loading curve using the Derjaguin–Muller–

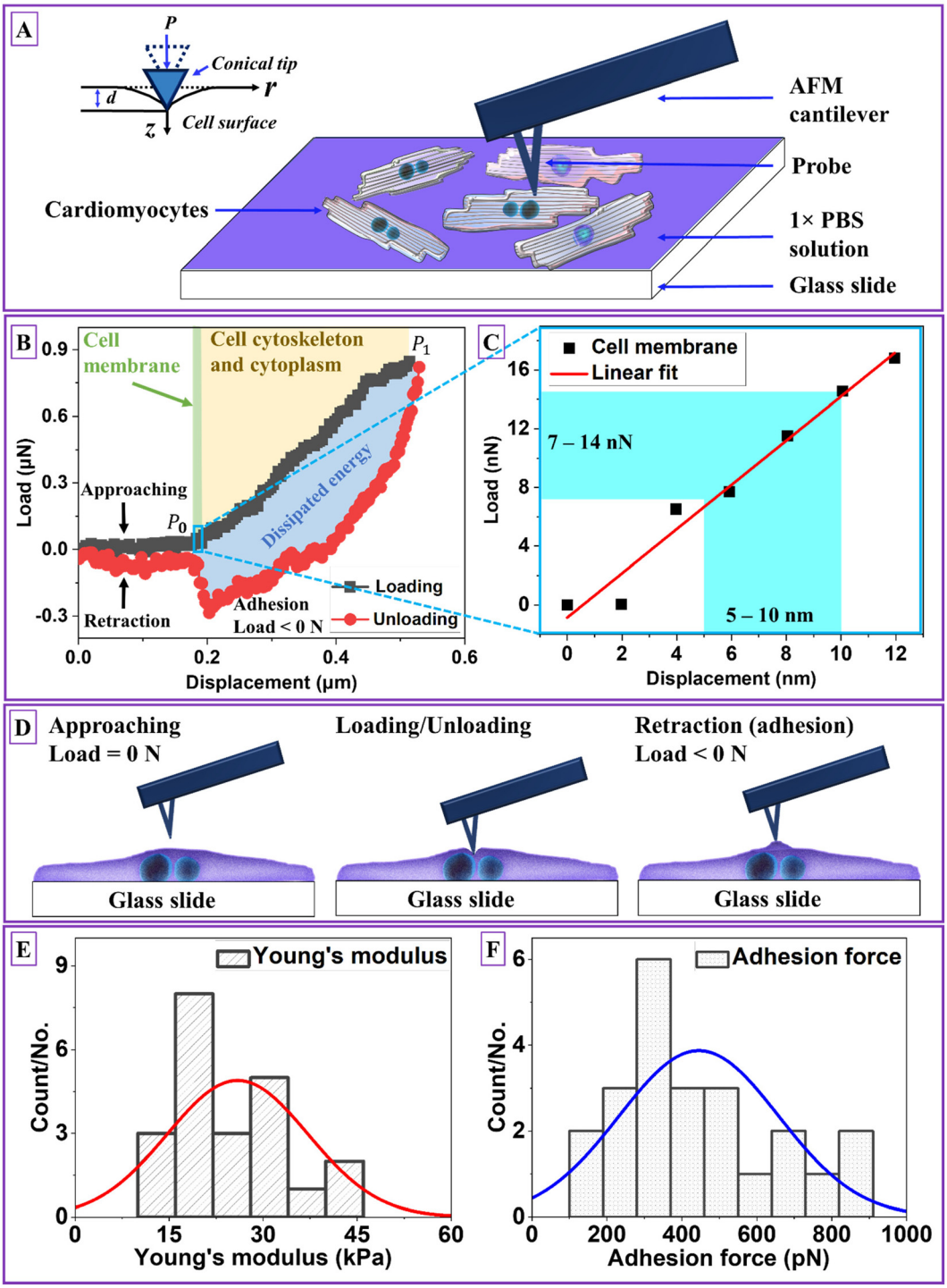


**Fig. 1** Single hiPSC-CM mechanical property measurement. (A) A schematic of AFM nanoindentation on alive hiPSC-CMs (D4) seeded on a glass slide using a conical probe, (B) load–displacement curve of the AFM indentation process, including approaching, loading, unloading, and retraction ($n$ = 50, 25 cells), (C) the initial linear stage with displacement within 10 nm corresponding to detected cell membrane load of 7–14 nN ($n$ = 50, 25 cells), (D) a schematic of the nanoindentation process and the corresponding cell–probe interaction statuses, (E) the detected Young's modulus distribution of single hiPSC-CM, and (F) the detected adhesion force distribution of single hiPSC-CM. Note: D4 means hiPSC-CMs were measured after they started beating for four days.

Toporov (DMT) model[28,36] (eqn (3)). According to Garcia *et al.*,[27,37] the force equation for a conical probe of half-angle $\theta$ of 10° is eqn (4):

$$F(I) = \frac{4}{3}\frac{E'}{1-\nu^2}\sqrt{R}I^{3/2} - 4\pi R\Delta\gamma \quad (3)$$

$$F[I] = \frac{8\tan\theta}{3\pi}E'I^2 + 0.721\frac{8\tan^2\theta}{3\pi d}E'I^3 + 0.650\frac{8\tan^3\theta}{3\pi d^2}E'I^4 + O\left(\frac{I^5}{d^3}\right) \quad (4)$$

where $F$ is the load, $d$ is the indentation depth, $R$ is the tip radius, $\Delta\gamma$ is surface energy, and $E'$ is calculated using eqn (S1) (in the ESI†). As shown in Fig. 1E, $E'$ ranged from 14–57 kPa with an average value of 25.93 ± 11.24 kPa. The captured de-adhesion force between the probe and hiPSC-CM ranged from 100–1000 pN with an average value of 445.27 ± 212.97 pN (Fig. 1F), correlating to the disruption of hydrogen bonds (H-band) and/or van der Waals (VdW) forces between the AFM probe and hiPSC-CM membrane phospholipids.[38]

Garcia *et al.*[28] differentiated viscoelastic descriptions into two steps: (1) mechanical-equivalent models or continuum mechanics theories, and (2) transform deflection into tip–sample distance relationships. Using the acquired elastic modulus and viscoelasticity of hiPSC-CMs, we modeled the von Mises stress distribution near the indentation region using the finite element method. The Mooney–Rivlin two-parameter model and two-generalized Maxwell branches were applied to simulate hiPSC hyperelasticity and viscoelasticity, respectively. The stress and strain were computed using a strain energy density function $W_s$ (eqn (5)):

$$W_s = C_{10}(\bar{I}_1 - 3) + C_{01}(\bar{I}_1 - 3) + \frac{1}{2}\kappa(J_{el})^2 \quad (5)$$

where $C_{10}$ and $C_{01}$ are empirically determined material constants, $\bar{I}_1$ is the isochoric first invariant, $\kappa$ is the bulk modulus, and $J_{el}$ is the elastic volume ratio. As shown in Fig. S1,† the von Mises stress accumulated at the center of the probe progressively propagated into the cytoskeleton, leading to the invagination of the cell membrane and the flow of cytoplasm. Invagination in biology describes the phenomenon of exterior membrane folding into a cavity. Hysteresis was shown as a stress lag after probe–cell separation. The modeling result mimics hiPSC-CM mechanical behavior intermediate deformation mechanism corresponding to the load–displacement curve shown in Fig. 1B, contributing to a more comprehensive understanding of cell mechanics. Predictably, local mechanics of biomaterials that mimic the elastic modulus and viscoelasticity of hiPSC-CMs can provide appropriate mechanical support for their growth and functions.

### HiPSC-CM adhesion behaviors

The fluidic micropipette technique[22] combines AFM with micro-channeled cantilevers with tunable nano- or micro-sized apertures (Fig. 2A), allowing single-cell isolation, injection or deposition materials, and adhesion characterization. The test was performed by approaching a targeted hiPSC-CM with a 1× PBS-filled cantilever (Fig. 2B). Sucking was applied under negative pressure of ≤1 bar upon aperture reaching and right above the cell surface, corresponding to a load of 0 N (Fig. 2C). After the hiPSC-CM membrane was tightly contacted within the aperture, a small load of 15–45 nN was observed. The targeted cell was detached by retracting the cantilever, correlating to the isolating process with a load < 0 N (red curves). The minimum force during the isolating process was pull-off or adhesion force. The load–displacement curve represented the intermediate force changing and deformation mechanism corresponding to the measurement process, as shown in Fig. 2D and E. Video V1† shows the hiPSC-CM pull-off process.

The pull-off force between hiPSC-CM and glass substrate (Fig. 2F) was 100–210 nN with an average value of 167.58 ± 22.56 nN. The adhesion force between two hiPSC-CMs was 50–100 nN with an average value of 79.22 ± 10.80 nN, attributed to gap junctions, desmosomes, and tight junctions (Fig. 2G). The gap and tight junctions are strong mechanical connections linked to the cytoskeleton, regulating intercellular force and signal transmission and influencing cell regulatory and migratory behaviors.[3] Additionally, cadherins,[39] integrins, nectins, and junctional adhesive molecules are in charge of the physical cell–cell linkage. The functions of these molecules are regulating intercellular communication and signaling.[39] It indicates that single-cell mechanics and cell–cell or cell–matrix adhesion might be directly correlated. Due to adhesive contact, there is pressure at the interface (Fig. 2H). The interface energy ($\gamma$) is the dissipation energy during the approaching–contact–detaching process, which is calculated by eqn (6):

$$\gamma = \int_{s_{min}}^{s_{max}} F(s)\mathrm{d}s \quad (6)$$

where $s_{min}$ and $s_{max}$ are the minimum and maximum displacement and $F(s)$ is the load–displacement curve. $\gamma$ of two hiPSC-CMs and between hiPSC-CM and glass substrate was 0.45 ± 0.07 and 0.58 ± 0.11 pJ, respectively.

The cell–cell adhesion force during the detaching process was nonlinear, with a rapid decrease at the initial stage, as plotted in Fig. 2I. We hypothesized that cell–cell adhesion exhibits viscoelastic behavior due to structure connections with cell structural building blocks. To prove that we extracted the data for viscoelastic modeling using eqn (7):

$$F(t) = \frac{4}{3(1-\mu_{\text{hiPSC-CM}}{}^2)}\sqrt{R}d^{\frac{3}{2}}(t)\int_0^t E(t-t')\mathrm{d}t' \quad (7)$$

where $E(t)$ is the relaxation modulus. The viscoelastic behavior was fitted by the Prony series model,[40] composed of a linear spring and three parallel Maxwell units, which gives eqn (S2) (in the ESI†). As shown in Fig. 2I, the time-dependent adhesion force curve was fit well by eqn (S2)† with $R^2$ of 0.97 and the fitting curve of $F = -75.43 + 2.4 \times 10^5 \times e^{(-x/0.0011)} + 76.65\, e^{(-x/0.61)} + 18.88\, e^{(-x/0.033)}$. The corresponding viscosity coefficients $\eta_1$, $\eta_2$ and $\eta_3$ are $2.4 \times 10^5$, 76.65, and 18.88 Pa s, respectively, determining the time-dependent energy dissipa-

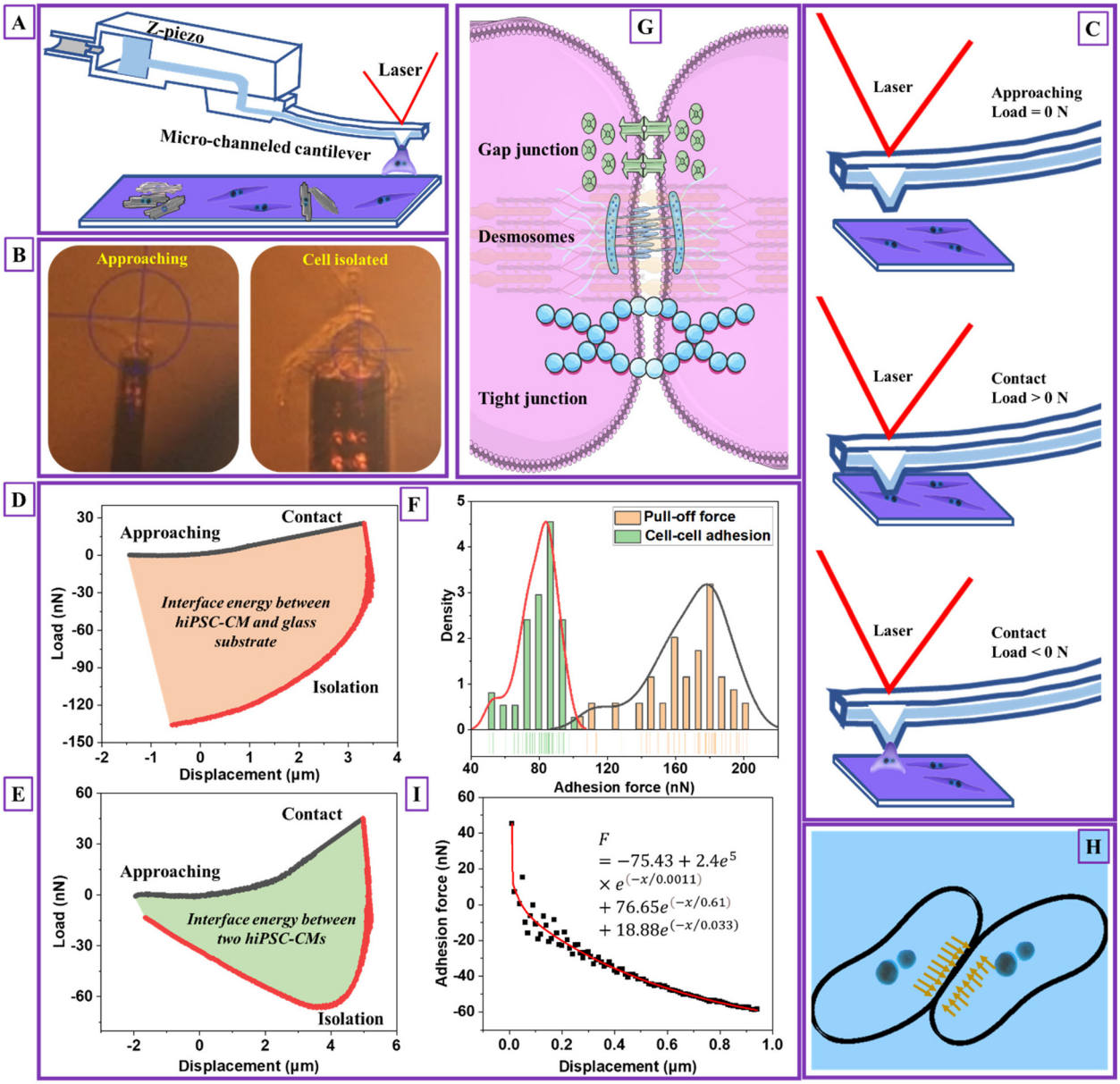


**Fig. 2** Cardiomyocyte–cardiomyocyte (D4) adhesion measurement. (A) Schematic images of detaching one single hiPSC-CM and measuring adhesion between two hiPSC-CMs' process, (B) the images of practical detaching one single hiPSC-CM and measuring adhesion between two hiPSC-CMs' process, (C) a schematic of hiPSC-CM adhesion detection process and the corresponding cell–micropipette interaction statuses, (D) load–displacement curve of detaching one single hiPSC-CM process ($n$ = 50, 25 cells), (E) load–displacement curve of measuring adhesion between two hiPSC-CMs' process ($n$ = 50, 25 cells), (F) the detected cardiomyocyte–cardiomyocyte adhesion force distribution and pull-off force distribution when detaching one single hiPSC-CM from the glass substrate, (G) a schematic of cardiomyocyte–cardiomyocyte adhesion mechanism, (H) a schematic of cardiomyocyte–cardiomyocyte adhesion and compression distribution at the contact region, and (I) the fitted cell–cell adhesion force during the initial detaching process using the Prony series model (the black scatters are extracted from the initial unloading curve from Fig. 2E with unchanged load and modified displacement values. The modification considers the start unloading point with a displacement of 0. The data from the initial 0–1 μm unloading section is used for data modeling. The raw and treated data is attached in an Excel sheet, see ESI†). Note: D4 means hiPSC-CMs were measured after they started beating for four days.

tion rate. Specifically, $\eta_1$ associated with the first Maxwell unit, characterizing the material's short-term (high frequency) viscosity. Corresponding, $\eta_2$ and $\eta_3$ associated with the second and third Maxwell units, representing intermediate-term (middle frequency) and long-term (low-frequency) materials viscosity. A lower value of $\eta_1$ compared to $\eta_2$ and $\eta_3$ indicates less resistance to deformation due to elasticity of cell membrane during the initial indentation process. Moreover, the inequality $\eta_1 < \eta_3 < \eta_2$ suggests the frequency-dependent viscoelastic behavior[28] with a stronger viscous response at higher

 

frequencies and a relatively weaker viscous response at intermediate frequencies. The viscoelastic behavior of cell–cell adhesion verifies our hypothesis that its intimate association with single-cell mechanics is due to linkages between cell–cell junctions and the cytoskeletons. The adhesion and viscoelasticity research highlighted the importance of fabricating biomaterials with adhesive molecules and proteins to support cardiomyocytes' electrical and chemical coupling. It is worth noting that the geometry of the micropipette is circular with a flat aperture of 4 μm in diameter. The limitation of this modeling is not considering the effect of micropipette geometry and contact area.[28]

### Single hiPSC-CM contractility

Spontaneous cardiomyocyte (CM) contractility[41] is the chemical–electrical–mechanical composite process controlled through the gap junctions of intercalated discs *via* excitation–contraction coupling. Therefore, contractility behavior, including beating rate, rhythm, and full-field strain map, directly reflects CM functions and maturation, determined by physiological structure, mechanics, gene expression, and metabolism.[13] A dimensionless factor defines cell shape $s_c$ ($0 \leq s_c \leq 1$) using eqn (S3) (in the ESI†). $s_c$ closes to 0 and 1 representing circle and rectangular. As shown, hiPSC-CMs with rounded (Fig. 3A) and elongated rectangular shapes (Fig. 3B) were observed on glass and PDMS substrates, where the corresponding $s_c$ was 0.25 and 0.75, respectively. Compared to a randomly distributed structure, the elongated shape exhibited a highly aligned myofibrillar cytoskeleton and T-tubule (Fig. 3C), contributing to maturation, calcium metabolism, and contractile anisotropy.[41] T-tubules and spontaneous rhythmic beating are indirect evidence of energy metabolism, electrophysiological maturation, and gene expression of $Ca^{2+}$ channels relating to its physiological condition.

The DIC technique characterized the full-field contractile-related deformation, revealing spatiotemporal beating frequency, rhythm, and magnitude. The time-dependent principal strains ($e_1$) calculated from tracked displacements were shown in Fig. 3D and E, which play a critical role in showing CM homeostasis.[13] HiPSC-CMs seeded on the glass substrate displayed an inhomogeneous beating rhythm. The time-dependent displacements (Fig. 3F and G) along the *x*- and *y*-direction were analyzed to compare the contractile anisotropy. Nearly 2–3 times lower in *y*-direction displacement magnitude than that of *x*-direction was observed with a consistent abnormal rhythm similar to strain. The time-dependent $e_1$ color maps at the systole and diastole phases are plotted in Fig. 3H and I, where blue/purple and yellow/red are denoted as contraction and dilation, respectively. HiPSC-CMs seeded on the PDMS substrate demonstrated more uniformity in the diastole phase than in glass. Videos V2 and V3† show the bright-field beating and DIC analyzed the major principal strain ($e_1$) videos of hiPSC-CM seeded on cover glass (250×), respectively. Videos V4 and V5† show hiPSC-CM seeded on PDMS substrate (250×). We observed substrate-stimulated hiPSC-CM shape differences, inhomogeneous/homogenous beating rhythm, and contractile anisotropy. Myocyte is the major contributor to heart contractility, where spontaneous beating is directly associated with heart abnormalities. For example, cardiac electrophysiologists monitor heart rhythm using a 12-lead electrocardiogram to check heart attack, failure, ischemia, myocardial infarction, and arrhythmia. It indicated that hiPSC-CM morphology–contractile-pathology is tightly interrelated.

We hypothesized that contractile-related $e_1$ could be linked to the detected viscoelasticity measured by AFM We analyzed the left half cycle of $e_1$, which fitted with the Kelvin–Voigt viscoelastic model[42] using eqn (S4) (in the ESI†). Due to the spontaneous contractile being recorded and not detected by the AFM probe, there is no need to introduce tip geometry. The fitting curve for hiPSC-CM seeded on the glass substrate (Fig. 3J) exhibited an $R^2$ of 60% and an equation of $\varepsilon(t) = 71.40 + 71.80\ \exp\left(-\frac{t}{2.17}\right)$. The fitting results for hiPSC-CM seeded on the PDMS substrate (Fig. 3K) demonstrated an $R^2$ of 97.40% with the equation of $\varepsilon(t) = 0.36 + 0.26\ \exp\left(-\frac{t}{0.077}\right)$. The viscosity coefficients of hiPSC-CM seeded on glass and PDMS substrates are 71.80 and 0.26 Pa s, respectively. This suggests that hiPSC-CM seeded on the glass substrate is more resistant to spontaneous contractile deformation with prominent viscous behavior. The data proved our hypothesis and suggested that substrate stiffness[8] influences hiPSC-CM viscoelasticity. Typically, hiPSC-CM maturation on soft substrates reduces viscosity, attributed to alterations in cytoskeletal organization, expressions of proteins involved in cell adhesion and mechanotransduction, and contractile–structure associations. Actin, myosin, troponin, tropomyosin, nebulin, and titin are major proteins involved in the contractile of cardiomyocytes.[43] These proteins are the building blocks of thin and thick myofilaments, intertwining with cytoskeletal networks to support contractility.[43] To calculate the strain-related beating force, we fitted the force–strain curve (Fig. 3L), exhibiting an $R^2$ of 99.46% with the equation of $\varepsilon(t) = 1.03 + 1.04\ \exp\left(-\frac{t}{0.17}\right)$. The calculated time-dependent beating force for hiPSC-CM seeded on the PDMS substrate is plotted in Fig. 3M, revealing a maximum force at systole and diastole phases of ~0.01 and ~0.15 ± 0.02 μN. Therefore, we successfully connected hiPSC-CM anamorphism with contractile forces using non-invasive DIC and AFM nanoindentation techniques, which quantitatively characterize a biomechanical phenomenon using force rather than biological descriptive, modeling or "biased" invasive methods.[1,2] The importance of hiPSC-CM contractility is the guidance of designing nN–μN force responsive biomaterials for cardiac bioengineering.

In summary, we endeavor to test the feasibility of constructing a hiPSC-CM mechanic's testbed to address numerous myocardial physiology and pathophysiology issues. Three technologies, including AFM nanoindentation, fluidic micropipette, and DIC technique, were employed to study single hiPSC-CM

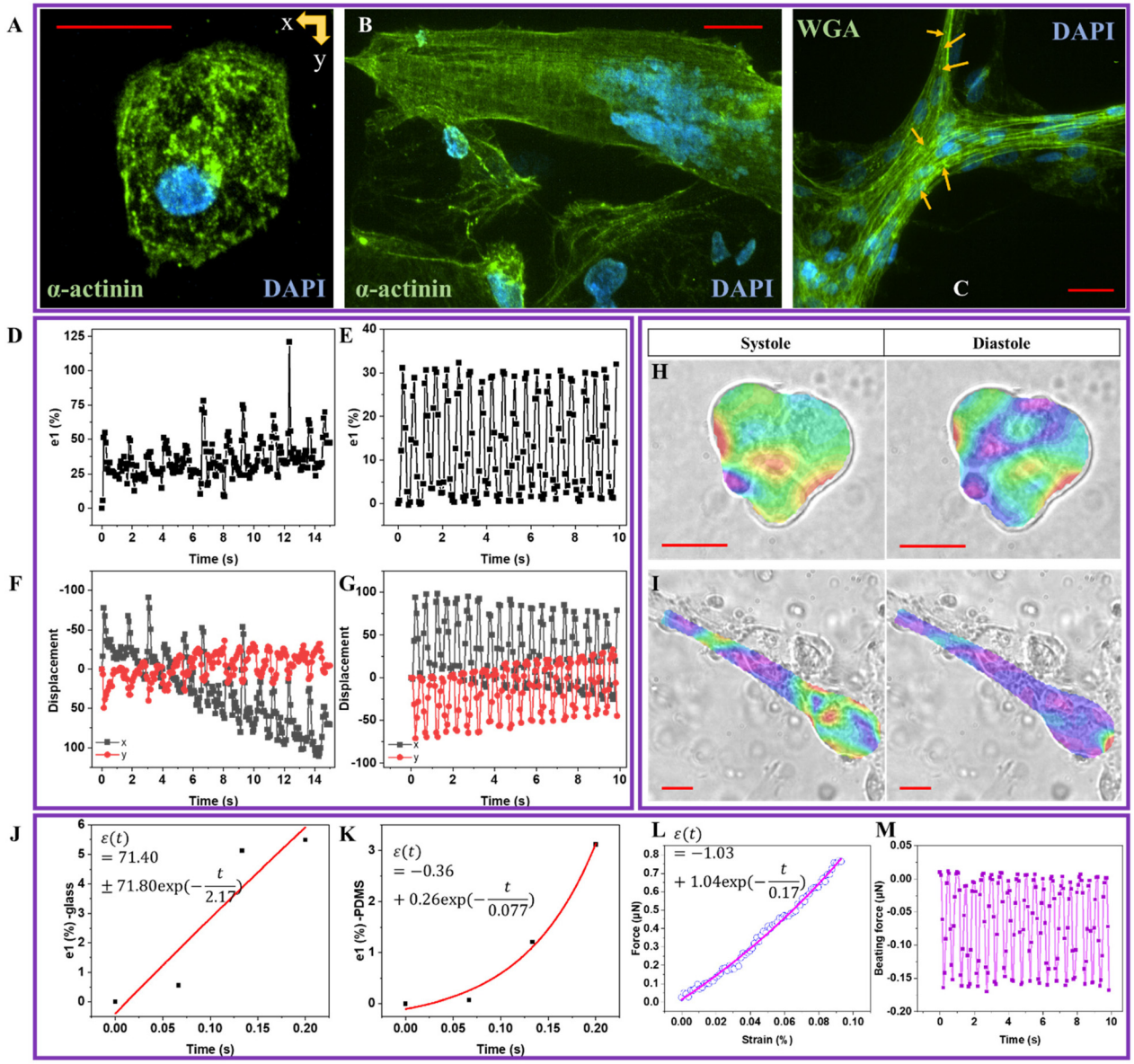


**Fig. 3** Single hiPSC-CM (D4) structure and beating mechanics. (A) Confocal image of single hiPSC-CM on glass slide with α-actinin stained with green color and hiPSC-CM nucleus stained with blue color, (B) confocal image of single hiPSC-CM on polydimethylsiloxane (PDMS) substrate with α-actinin stained with green color and hiPSC-CM nucleus stained with blue color, (C) immunofluorescence confocal images with T-tubule strained with WGA and green color and hiPSC-CM nucleus stained with blue color, (D) time-dependent major principal strain ($e_1$, %) of single hiPSC-CM on glass slide, (E) time-dependent *x*-direction displacement (*x*, μm) and *y*-direction displacement (*y*, μm) waves of single hiPSC-CM on glass slide ($n$ = 6, 3 cells), (F) time-dependent major principal strain ($e_1$, %) of single hiPSC-CM on PDMS substrate ($n$ = 6, 3 cells), (G) time-dependent *x*-direction displacement (*x*, μm) and *y*-direction displacement (*y*, μm) waves of single hiPSC-CM on PDMS substrate ($n$ = 6, 3 cells), (H) $e_1$ maps of single hiPSC-CM on glass slide at systole and diastole phases, (I) $e_1$ maps of single hiPSC-CM on PDMS substrate at systole and diastole phases, (J) the fitting curve of the left half cycle of $e_1$ for hiPSC-CM seeded on the glass substrate using the Kelvin–Voigt viscoelastic model, (K) the fitting curve of the left half cycle of $e_1$ for hiPSC-CM seeded on the PDMS substrate using the Kelvin–Voigt viscoelastic model, (L) the fitting curve of loading curve acquired in the AFM nanoindentation test, and (M) the time-dependent beating force curve for hiPSC-CM seeded on the PDMS substrate. Note: D4 means hiPSC-CMs were measured after they started beating for four days. The scale bar size is 25 μm.

Young's modulus, model deformation mechanism, probe cell adhesion and interface energy, and measure beating mechanics. The results demonstrated that the cytoskeleton's viscoelasticity dominated single hiPSC-CM mechanics with a visible energy dissipation characteristic. The adhesion force between two hiPSC-CMs was primarily governed by gap and tight junctions that directly link with their cytoskeletons and single-cell mechanics, manifesting by its viscoelastic behavior that fits perfectly with the Prony series model. Distinct morphology and time-dependent beating mechanics were observed for hiPSC-CM seeded on glass and PDMS substrate. The time-dependent contractile strain for hiPSC-CM seeded on PDMS

 

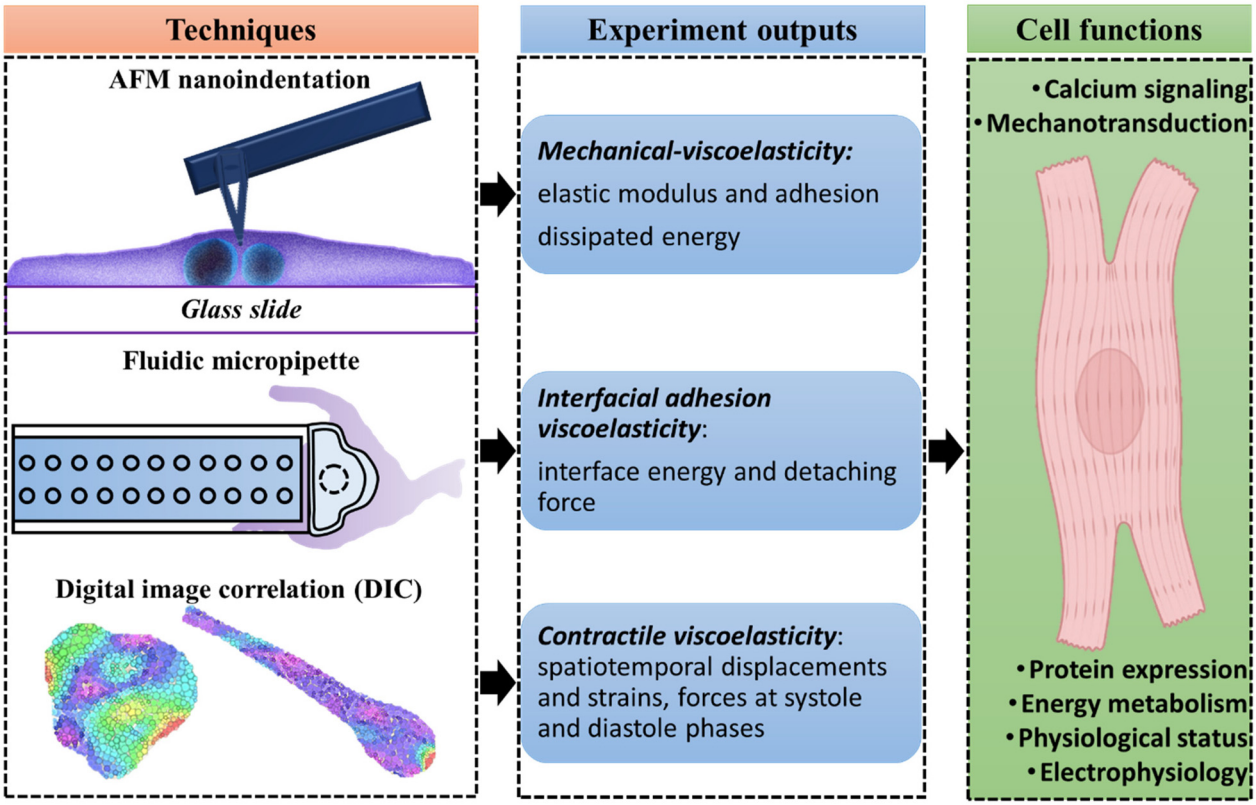


**Fig. 4** The associations of mechanic's testbed and hiPSC-CM functions. The experiment outputs of AFM nanoindentation are elastic modulus and adhesion between the probe and hiPSC-CM. The outputs of the fluidic micropipette are interface energy and detaching force. The outputs of beating mechanics analyzed by the DIC technique are spatiotemporal displacements, strains, and forces at the systole and diastole phases. The experiment outputs directly associate with hiPSC-CM mechanotransduction, maturation, homogeneity, metabolism, gene expression, and physiological status.

substrate also exhibited viscoelasticity, indicating substrate stiffness is essential in maintaining hiPSC-CM functions. Contractile associated with electrical and mechanical stimuli are determined by beating-related proteins' expression, maturation of ion channels, calcium signaling, and energy utilization.[41] These factors are also critical for the functional characteristics of cardiomyocytes, including propagating electrical signaling and performing structural and mechanical integrity.[44] Therefore, this study disclosed associations between cardiomyocyte contractile and functional properties. Most importantly, our study revealed robust structural–mechanical–viscoelasticity, demonstrating the potential practicality of our mechanical platform conception, as illustrated in Fig. 4.

## Conclusions

The viscoelasticity of cardiomyocytes and the underlying structural–mechanical–functional mechanism lack systematic study, although it is critical for cardiac functions. This study investigated a single cardiomyocyte's spatiotemporal mechanical and viscoelastic behaviors using three cutting-edge technologies: AFM nanoindentation, fluidic micropipette, and DIC Our results showed a detected cytoplasm load and dissipated energy of 7–14 nN and 55.75 ± 7.98%, indicating hiPSC-CM's mechanics and viscoelasticity is intimately linked with cytoskeleton network, intracellular structures, and extracellular matrix. The detected adhesion force between two hiPSC-CMs was 50–100 nN with an interface energy of 0.58 ± 0.11 pJ, attributing to cell interfacial molecular connections, including cadherins and gap/tight junctions. Based on the acquired data, we modeled cell–cell adhesion and contractility, demonstrating the fundamental role of cardiomyocyte mechanics and time-dependent viscoelasticity in organizing and maintaining its electrical and mechanical integrations with the surrounding environment. Overall, this study highlights the viscoelasticity of cardiomyocytes and its essential inter-relationship with internal structure, contractile, and functions, contributing to designing biomaterials with mimicked force response mechanisms as that of cardiomyocytes.

## Materials and methods

### HiPSC culture and cardiomyocyte differentiation

HiPSCs (human iPSCs from reprogrammed fibroblasts, GM23338) were purchased from Coriell Institute for Medical Research and grown on Matrigel-coated plates (B.D.

Biosciences) in stem basal medium (mTeSR1, STEMCELL Technologies) for about 7 days to reach 80–90% of confluence. On day 0, hiPSCs were treated with CHIR99021 (12 μM, Tocris, 4423) diluted in RPMI/B27 – insulin for 24 hours, and the media changed every day until day 3. On day 3, hiPSCs were treated with IWP4 (5 μM, Tocris, 5214) mixed with RPMI/B27 – insulin, which was removed on day 4. The medium was changed every other day. From day 9, hiPSCs were maintained in RPMI/B27 containing insulin with regular medium change. Spontaneous contractions were observed between 10 to 12 days.

### Seeding hiPSC-CM

The cover glass was incubated with 10 μg $ml^{-1}$ of human fibronectin (Corning, 356008) in sterile phosphate-buffer solution (1× PBS, Gibco) for 1 hour at 37 °C and rinsed with sterile 1× PBS. HiPSC-CMs were digested from tissue culture plates by adding TrypLE express enzyme (Gibco, 12605010) at 37 °C for 15 minutes. The detached cells were resuspended in RPMI/B27 containing insulin. HiPSC-CMs were replanted on cover glass-fibronectin coated at a density of $3 \times 10^5$ cells with RPMI/B27 containing insulin, fetal bovine serum (10%, Gibco, 10099141), pen strep (1%, Gibco, 15140148) and Y-27632 (5 μM, Tocris, 1254) for 48 hours. On day 3, hiPSC-CMs were maintained in RPMI/B27 containing insulin. Spontaneous contractions were observed between 7 to 9 days.

### Immunostaining and immunofluorescence imaging

HiPSC-CMs seeded on the cover glass were prepared for immunocytochemical analysis on day 4 after the spontaneous beating started. The cells were immersed in paraformaldehyde (4%) for 20 minutes, blocked, and permeabilized with Triton X-100 (0.2%) and bovine serum albumin (1%) in 1× PBS for 20 minutes at room temperature. Cells were stained overnight with the primary antibody, anti-sarcomeric α-actinin (Abcam, 1 : 300 dilution). Samples were incubated with goat anti-mouse secondary antibody Alexa-488 for 40 minutes (Abcam, 1 : 300 dilution), followed by 10 minutes incubation with 4′,6-diamidino-2-phenylindole (DAPI) (Invitrogen, 30 nM). For T-tubule labeling, the samples were incubated with WGA-Alexa Fluor 488 (Life Technologies, W11261) for 10 min and rinsed with 1× PBS. Fluorescence images were acquired using the confocal microscope (Nikon ECLIPSE Ti2) with a 60× objective.

### Mechanics of hiPSC-CM measured by AFM

HiPSC-CM cell mechanics were measured using AFM (Nanosurf FlexAFM, Liestal, Switzerland). HiPSC-CMs were seeded on cover glasses with a diameter of 15 mm and incubated at 37 °C. Before the measurements, the cover glass was transferred to a thin flat microscope slide. Cantilever Tap150Al-G (NanoANDMore, Watsonville, CA) with length, width, resonant frequency, stiffness, half-cone angle, and tip radius of 125 μm, 25 μm, 150 kHz, 5 N $m^{-1}$, 10° at the apex, and <10° was selected for single cell mechanic measurements. The spring constant was calibrated using the frequency sweep method using Nanosurf C3000 software before deflection and crosstalk calibrations. The nanoindentation test was performed at the Spectroscopy mode using static force, force–distance spectroscopy grid, and data point 1024. The load–displacement curve was analyzed by Nanosurf ANA software, where Derjaguin–Muller–Toporov (DMT) model was applied for Young's modulus calculation. The minimum backward force was the adhesion force between the probe and hiPSC-CM, verifying contact. Fifty tests on 25 cells were performed, where the data was denoted as mean ± standard deviation.

### Adhesion force measurement

The adhesion forces between hiPSC-CM and glass slide or between two hiPSC-CMs were measured using micropipette cantilevers (Cytosurge AG, Opfikon, Switzerland) with a circular and flat aperture of 4 μm in diameter and spring constant of 2 N $m^{-1}$. The fluidic channel of the micropipette cantilever was filled with 1× PBS (5 μl) using a hand-held pipette (2–20 μl). It was mounted to the head of the AFM, whereas the Nanosurf AFM system was mounted on an inverted microscope (Carl Zeiss, Germany). After manual laser alignment, the micropipette cantilever's spring constant and deflection sensitivity were calibrated using the thermal tuning and Cytosurge software. Before the measurement, the hiPSC-CM seeded glass was transferred to a Petri dish filled with 1× PBS. The test was completed within 1.5 h to avoid cell death. A hiPSC-CM was selected, approached, and sucked under a pressure of 600–800 mbar for 10 s to ensure the sealing of the cell to the cantilever. The cantilever is retracted using a speed of 1 μm $s^{-1}$ to isolate hiPSC-CM. The load–displacement curve was analyzed by Nanosurf ANA software, where the adhesion force and interface energy were analyzed. Fifty tests on 25 cells were performed, where the data was denoted as mean ± standard deviation.

### Bright-field imaging and DIC analysis

HiPSC-CMs seeded on cover glass or PDMS substrate were removed from the incubator and placed on the inverted microscope with 40× objective and a C.C.D. camera (FLIR, Grasshopper3 GS3-U3-15S5M) for bright-field beating video recording. The video with a frame rate of 15. The video was converted into sequential images for DIC analysis using VIC-2D software (Correlated Solutions, Irmo, SC). The initial image was selected as the reference, with all others as deformed images. The applied subset and step size were 51 and 8, where the corresponding displacements as of the reference image were analyzed for each frame. The time-dependent *x*- and *y*-directional displacement, principal strain, and strain maps were acquired for beating mechanics analysis.

## Author contributions

A. A. and L. L. designed the concept of the work. A. S. R. and J. H. performed hiPSC-CM differentiation, culture, staining, imaging, and corresponding protocol writing. L. L. performed AFM nanoindentation, micropipette, and DIC analysis. The

 

manuscript was written by L. L. and A. A. All authors have approved the final version of the manuscript.

## Conflicts of interest

The authors declare no conflict of interest.

## Acknowledgements

This work was supported by the Engineering Research Centers Program of the National Science Foundation under N.S.F. Cooperative Agreement no. EEC-1647837. The authors acknowledge Mr B. Aguiar's support in supplementary Video V1† editing.

## References

1 S. R. Heidemann and D. Wirtz, *Trends Cell Biol.*, 2004, **14**, 160–166.
2 D. A. Fletcher and R. D. Mullins, *Nature*, 2010, **463**, 485–492.
3 M. A. Caporizzo and B. L. Prosser, *Nat. Rev. Cardiol.*, 2022, **19**, 364–378.
4 L. Lou, K. O. Lopez, P. Nautiyal and A. Agarwal, *Adv. NanoBiomed Res.*, 2021, **1**, 2100075.
5 C. A. Blair and B. L. Pruitt, *Adv. Healthcare Mater.*, 2020, **9**, 1901656.
6 M. Mathelié-Guinlet, F. Viela, J. Dehullu, S. Filimonava, J. M. Rauceo, P. N. Lipke and Y. F. Dufrêne, *Commun. Biol.*, 2021, **4**, 1–8.
7 L. Wang, W. Dou, M. Malhi, M. Zhu, H. Liu, J. Plakhotnik, Z. Xu, Q. Zhao, J. Chen and S. Chen, *ACS Appl. Mater. Interfaces*, 2018, **10**, 21173–21183.
8 A. J. Ribeiro, Y.-S. Ang, J.-D. Fu, R. N. Rivas, T. M. Mohamed, G. C. Higgs, D. Srivastava and B. L. Pruitt, *Proc. Natl. Acad. Sci. U. S. A.*, 2015, **112**, 12705–12710.
9 K. Dasbiswas, S. Majkut, D. Discher and S. A. Safran, *Nat. Commun.*, 2015, **6**, 1–8.
10 L. Lou, T. Paul, B. A. Aguiar, T. Dolmetsch, C. Zhang and A. Agarwal, *ACS Appl. Mater. Interfaces*, 2022, **14**, 42876–42886.
11 L. Lou, L. Paolino and A. Agarwal, *ACS Appl. Mater. Interfaces*, 2023, 24197–24208.
12 A. Shinde, K. Illath, P. Gupta, P. Shinde, K.-T. Lim, M. Nagai and T. S. Santra, *Cells*, 2021, **10**, 577.
13 D. J. Shiwarski, J. W. Tashman, A. Tsamis, J. M. Bliley, M. A. Blundon, E. Aranda-Michel, Q. Jallerat, J. M. Szymanski, B. M. McCartney and A. W. Feinberg, *Nat. Commun.*, 2020, **11**, 1–15.
14 Q. Zheng, M. Peng, Z. Liu, S. Li, R. Han, H. Ouyang, Y. Fan, C. Pan, W. Hu and J. Zhai, *Sci. Adv.*, 2021, **7**, eabe7738.
15 M. S. Ma, S. Sundaram, L. Lou, A. Agarwal, C. S. Chen and T. G. Bifano, *Front. Bioeng. Biotechnol.*, 2023, **11**, 703.
16 A. Sesena-Rubfiaro, N. J. Prajapati, L. Paolino, L. Lou, D. Cotayo, P. Pandey, M. Shaver, J. D. Hutcheson, A. Agarwal and J. He, *ACS Biomater. Sci. Eng.*, 2023, 1644–1655.
17 L. Lou, A. S. Rubfiaro, J. He and A. Agarwal, *Adv. Mater. Technol.*, 2021, **6**, 2100669.
18 H. Li, S. Sundaram, R. Hu, L. Lou, F. Sanchez, W. McDonald, A. Agarwal, C. S. Chen and T. G. Bifano, *IEEE Trans. Biomed. Eng.*, 2023, 1–12.
19 K. H. Vining and D. J. Mooney, *Nat. Rev. Mol. Cell Biol.*, 2017, **18**, 728–742.
20 T. Panciera, A. Citron, D. Di Biagio, G. Battilana, A. Gandin, S. Giulitti, M. Forcato, S. Bicciato, V. Panzetta and S. Fusco, *Nat. Mater.*, 2020, **19**, 797–806.
21 T. Chowdhury, B. Cressiot, C. Parisi, G. Smolyakov, B. Thiébot, L. Trichet, F. M. Fernandes, J. Pelta and P. Manivet, *ACS Sens.*, 2023, 406–426.
22 O. Guillaume-Gentil, E. Potthoff, D. Ossola, C. M. Franz, T. Zambelli and J. A. Vorholt, *Trends Biotechnol.*, 2014, **32**, 381–388.
23 L. Lou, A. S. Rubfiaro, J. He and A. Agarwal, *Adv. Mater. Technol.*, 2021, 2100669.
24 T. Hattori, S. Shimizu, Y. Koyama, K. Yamada, R. Kuwahara, N. Kumamoto, S. Matsuzaki, A. Ito, T. Katayama and M. Tohyama, *Mol. Psychiatry*, 2010, **15**, 798–809.
25 E. Kardash, M. Reichman-Fried, J.-L. Maître, B. Boldajipour, E. Papusheva, E.-M. Messerschmidt, C.-P. Heisenberg and E. Raz, *Nat. Cell Biol.*, 2010, **12**, 47–53.
26 E. Kim, A. Lisby, C. Ma, N. Lo, U. Ehmer, K. E. Hayer, E. E. Furth and P. Viatour, *Nat. Commun.*, 2019, **10**, 1–17.
27 P. D. Garcia and R. Garcia, *Nanoscale*, 2018, **10**, 19799–19809.
28 R. Garcia, *Chem. Soc. Rev.*, 2020, **49**, 5850–5884.
29 G. Iribe, T. Kaneko, Y. Yamaguchi and K. Naruse, *Prog. Biophys. Mol. Biol.*, 2014, **115**, 103–114.
30 S. C. Lieber, N. Aubry, J. Pain, G. Diaz, S.-J. Kim and S. F. Vatner, *Am. J. Physiol.: Heart Circ. Physiol.*, 2004, **287**, H645–H651.
31 S. Deitch, B. Z. Gao and D. Dean, *MCB Mol. Cell. Biomech.*, 2012, **9**, 227.
32 T. Lanzicher, V. Martinelli, C. S. Long, G. Del Favero, L. Puzzi, M. Borelli, L. Mestroni, M. R. Taylor and O. Sbaizero, *Nucleus*, 2015, **6**, 394–407.
33 C. Zhang, W. Wang, W. He, N. Xi, Y. Wang and L. Liu, *Biophys. J.*, 2018, **114**, 188–200.
34 S. Kadota, L. Pabon, H. Reinecke and C. E. Murry, *Stem Cell Rep.*, 2017, **8**, 278–289.
35 V. Lulevich, T. Zink, H.-Y. Chen, F.-T. Liu and G.-y. Liu, *Langmuir*, 2006, **22**, 8151–8155.
36 B. V. Derjaguin, V. M. Muller and Y. P. Toporov, *J. Colloid Interface Sci.*, 1975, **53**, 314–326.
37 P. D. Garcia and R. Garcia, *Biophys. J.*, 2018, **114**, 2923–2932.
38 A. Viljoen, M. Mathelié-Guinlet, A. Ray, N. Strohmeyer, Y. J. Oh, P. Hinterdorfer, D. J. Müller, D. Alsteens and Y. F. Dufrêne, *Nat. Rev. Methods Primers*, 2021, **1**, 1–24.

39 B. M. Gumbiner, *Nat. Rev. Mol. Cell Biol.*, 2005, **6**, 622–634.
40 D. Gutierrez-Lemini, *Engineering Viscoelasticity*, Springer, Chambersburg, PA, 2014.
41 K. Ronaldson-Bouchard, S. P. Ma, K. Yeager, T. Chen, L. Song, D. Sirabella, K. Morikawa, D. Teles, M. Yazawa and G. Vunjak-Novakovic, *Nature*, 2018, **556**, 239–243.
42 M. Backholm, W. S. Ryu and K. Dalnoki-Veress, *Proc. Natl. Acad. Sci. U. S. A.*, 2013, **110**, 4528–4533.
43 B. L. Lin, T. Song and S. Sadayappan, *Compr. Physiol.*, 2011, 675–692.
44 K. Ronaldson-Bouchard, K. Yeager, D. Teles, T. Chen, S. Ma, L. Song, K. Morikawa, H. M. Wobma, A. Vasciaveo and E. C. Ruiz, *Nat. Protoc.*, 2019, **14**, 2781–2817.